Materials Today Bio 26 (2024) 101040

Contents lists available at ScienceDirect

Materials Today Bio

journal homepage: www.journals.elsevier.com/materials-today-bio

Self-assembled metal-phenolic nanocomplexes comprised of green tea catechin for tumor-specific ferroptosis

Min Wang [a], Aoling Yu [a], Wen Han [a], Jingyi Chen [b], Chunhua Lu [a,*], Xiankun Tu [b,**]

[a] MOE Key Laboratory for Analytical Science of Food Safety and Biology, Fujian Provincial Key Laboratory of Analysis and Detection Technology for Food Safety, College of Chemistry, Fuzhou University, Fuzhou, Fujian, 350116, China
[b] Department of Neurosurgery, Fujian Medical University Union Hospital, Neurosurgery Research Institute of Fujian Province, Fuzhou, Fujian, 350001, China

ARTICLE INFO

Keywords:
Epigallocatechin-3-gallate
Self-assembly
GSH depletion
H_2O_2 self-supplementation
Ferroptosis

ABSTRACT

Ferroptosis, a newly discovered form of regulated cell death, has garnered significant attention in the field of tumor therapy. However, the presence of overexpressed glutathione (GSH) and insufficient levels of H_2O_2 in the tumor microenvironment (TME) hinders the occurrence of ferroptosis. In response to these challenges, here we have constructed the self-assembled nanocomplexes (FeE NPs) utilizing epigallocatechin-3-gallate (EGCG) from green tea polyphenols and metal ions (Fe^{3+}) as components. After grafting PEG, the nanocomplexes (FeE@PEG NPs) exhibit good biocompatibility and synergistically enhanced tumor-inhibitory properties. FeE@PEG NPs can be disassembled by H_2O_2 in the TME, leading to the rapid release of Fe^{3+} and EGCG. The released Fe^{3+} produces large amounts of toxic •OH by the Fenton reactions while having minimal impact on normal cells. The generated •OH effectively induces lipid peroxidation, which leads to ferroptosis in tumor cells. Meanwhile, the released EGCG can autoxidize to produce H_2O_2, which further promotes the production of •OH radicals and increases lipid peroxide levels. Moreover, EGCG also depletes the high levels of intracellular GSH, leading to an intracellular redox imbalance and triggering ferroptosis. This study provides new insights into advancing anticancer ferroptosis through rational material design, offering promising avenues for future research.

1. Introduction

Ferroptosis, unlike apoptosis and necrosis, is an iron-dependent regulated pathway of programmed cell death involving iron-induced lipid peroxidation (LPO) [1–6]. It is initiated by the formation of highly toxic hydroxyl radicals (•OH) in the Fenton reaction. These •OH radicals can irreversibly trigger peroxidation of membrane lipids, leading to the accumulation of LPO and ultimately resulting in ferroptosis [7–12]. In recent years, iron-based nanomaterials such as ferroferric oxide, amorphous iron nanoparticles and iron organic frameworks have been extensively studied as inducers of ferroptosis, and their ability to induce •OH generation is believed to be responsible for achieving the therapeutic effect of ferroptosis [13–18]. Although the amount of H_2O_2 in the tumor microenvironment (TME) is typically much higher (around 100 μM) compared to normal tissues, endogenous H_2O_2 alone is still insufficient to induce ferroptosis [19–21]. Furthermore, the high expression of glutathione (GSH) (up to 2–10 mM), which acts as a scavenger of •OH, helps maintain redox homeostasis in tumor cells, thereby impeding the effectiveness of ferroptosis as a therapeutic strategy [22,23]. Therefore, increasing the level of H_2O_2 and depleting intracellular GSH may represent viable targets for achieving effective ferroptosis therapy in tumor cells.

The natural compound epigallocatechin-3-gallate (EGCG), major polyphenol in green tea, has demonstrated significant anticancer activity in both in vivo and ex vivo studies [24–26]. As a natural antitumor agent, EGCG inhibits tumor growth via anti-angiogenesis, inhibition of proliferation, and induction of apoptosis in tumor cells [27–29]. However, extensive research has revealed that EGCG suffers from issues such as instability, poor bioavailability, and a short half-life [30–32]. These characteristics make it unsuitable for effective biomedical applications in vivo. There have been studies using EGCG chelate with a variety of metal ions to prepare nanoparticles for the treatment of diseases [33–37]. However, EGCG is mostly used as a delivery vector, and the synergistic therapeutic effect of EGCG in the system has not been demonstrated. In addition to its antitumor activity, EGCG has been reported to function as a co-oxidant, promoting apoptosis by increasing

* Corresponding author.
** Corresponding author.
E-mail addresses: chunhualu@fzu.edu.cn (C. Lu), unionnstu@hotmail.com (X. Tu).

https://doi.org/10.1016/j.mtbio.2024.101040
Received 8 February 2024; Received in revised form 19 March 2024; Accepted 22 March 2024
Available online 24 March 2024

the level of H_2O_2 in tumor cells [38–42]. Furthermore, EGCG, which contains the gallate group, can act as a strong electrophilic reagent when oxidized to its benzoquinone form. It is capable of reacting with nucleophilic thiols (such as GSH), leading to the depletion of intracellular GSH [43,44].

Based on the strong inherent coordination between iron ions and polyphenols, we have successfully assembled Fe^{3+} and EGCG, and subsequently grafted them with PEG to create an H_2O_2-responsive ferroptosis-inducing platform (Fe-EGCG nanocomplexes, FeE@PEG NPs, Scheme 1). These carrier-free FeE@PEG NPs can be disassembled by H_2O_2 in TME, rapidly releasing EGCG and Fe^{3+}. The sustained supply of Fe^{3+} contributes to long-term cytotoxicity by catalyzing Fenton reactions, generating significant amounts of toxic •OH, while having minimal impact on normal cells. The generated •OH effectively induces lipid peroxidation, which leads to ferroptosis in tumor cells. Meanwhile, EGCG has the ability to autoxidize, producing H_2O_2, which further promotes •OH production and lipid peroxidation (LPO). Furthermore, EGCG depletes intracellular GSH, inhibits antioxidant systems, and disrupts the repair process of oxidized lipids, thereby triggering the accumulation of LPO. Overall, the coordinated assembly of green tea polyphenols and iron ions in the form of nanocomplexes presents a promising strategy for developing effective ferroptosis-inducing agents.

2. Materials and methods

2.1. Materials

Iron nitrate nonahydrate ($Fe(NO_3)_3•9H_2O$), epigallocatechin-3-gallate (EGCG), Polyethylene-polypropylene glycol (F-127), 5,5′-tetramethylbenzidine (TMB), o-dianisidine, 2,7-dichlorofluorescein diacetate (DCFH-DA) and horse radish peroxidase (HRP) were purchased from Sigma-Aldrich. 1,2-distearoyl-sn-glycero-3-phosphoethanolamine-N-[succinyl (polyethylene glycol)] (DSPE-PEG), and 5,5′-dithiobis-2-nitrobenzoic acid (DTNB) were purchased from Aladdin. N, N-dimethylformamide (DMF), ethanol, and H_2O_2 were purchased from Sinopharm Chemical Reagent Co., Ltd. Cell Counting Kit-8 (CCK-8) was purchased from Dojindo. GSH assay kit was purchased from Nanjing Jiancheng Bioengineering Institute. Mitochondrial membrane potential assay kit with 5,5′,6,6′-tetrachloro-1,1′,3,3′-tetraethylbenzimidazolylcarbocyani- ne iodide (JC-1), One-step TUNEL apoptosis assay kit, and Annexin V-FITC Apoptosis Detection Kit was purchased from Beyotime Biotechnology.

2.2. Synthesis of FeE NPs

DMSO solution of F-127 (20 mg/mL), EGCG (20 mg/mL), and $Fe(NO_3)_3•9H_2O$ (8 mg/mL), were prepared respectively. 200 μL F-127 solution, 200 μL EGCG solution and 158 μL $Fe(NO_3)_3$ solution were mixed and slowly added to the aqueous solution containing 5 mL PBS (total volume 20 mL), stirring at room temperature for 24 h. After the reaction was completed, the reaction solution was collected and centrifuged at 8000 rpm for 10 min. The centrifuge product was cleaned with water for 3 times to remove excess unreacted substances, and then dispersed in water to obtain uniformly dispersed FeE NPs aqueous solution.

2.3. Synthesis of FeE@PEG NPs

8 mg of DSPE-PEG was completely dissolved in 10 mL FeE NPs aqueous solution (0.2 mg/mL) by ultrasound for a certain time, and the mixture was stirred at room temperature overnight. After the reaction was completed, the solution was put into a centrifuge tube and centrifuged at 4 °C (8000 rpm, 10 min). The precipitate was cleaned with PBS for 3 times to obtain FeE@PEG NPs solution.

2.4. Extracellular depletion of GSH

The consumption of GSH was monitored by DTNB. PBS (control), H_2O_2 (10 mM), FeE@PEG NPs (100 μg/mL) and the mixture of H_2O_2 (100 μM) and FeE@PEG NPs (100 μg/mL) were mixed with GSH (10 mM) in PBS (pH = 7.4) and incubated at 37 °C for 30 min, respectively. Then each sample was centrifuged at 8000 rpm for 10 min. The supernatant of each sample was collected to evaluate the GSH level. After the co-incubation of the supernatant and DTNB (0.6 mg/mL) at 25 °C, the absorbance spectrum of each sample was measured by a UV–vis spectrometer.

2.5. Detection of extracellular H_2O_2

The o-dianisidine reagent was utilized for the analysis of H_2O_2 production. 100 μL o-dianisidine solution (10 mg/mL, in methanol) and 160 μL HRP solution (25 U/mol) were added to EGCG solution (0, 29, 58, 87, 116 μg/mL) and FeE@PEG NPs solution (0, 125, 250, 375, 500 μg/mL), respectively. And the mixed solutions were reacted at 37 °C. After reaction for1.5 h, 10 μL HCl (2 M) was added to terminate the

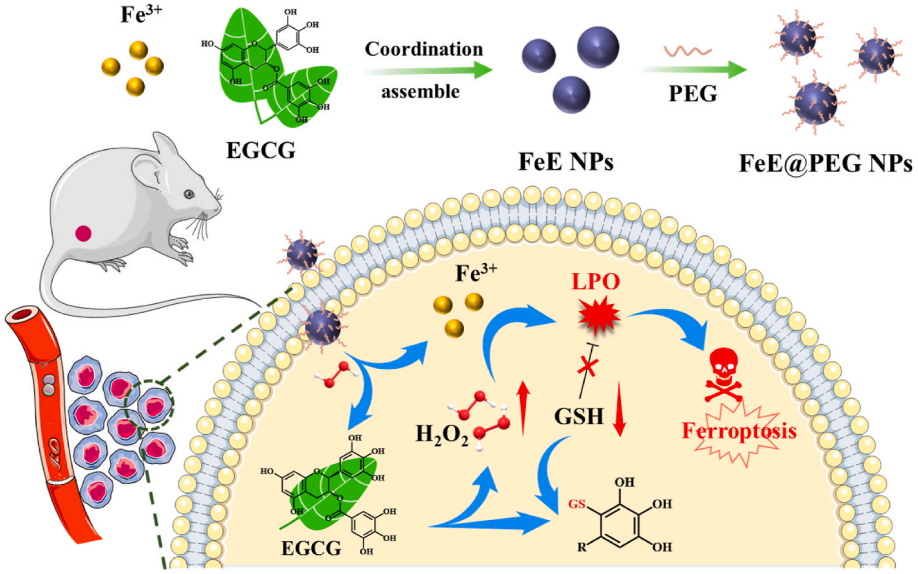

Scheme 1. Preparation of FeE@PEG NPs and schematic illustration of FeE@PEG NPs induced ferroptosis therapy.

reaction. The supernatant was obtained by centrifugation (8000 rpm, 10 min). The absorbance of the supernatant at 430 nm were detected through UV–vis spectroscopy. Based on the absorbance of standard concentration H_2O_2, the amount of H_2O_2 produced by EGCG and FeE@PEG NPs groups were calculated.

2.6. Detection of extracellular •OH

The chromogenic reaction of TMB was utilized for the analysis of •OH production. Briefly, TMB (0.8 mM) and FeE@PEG NPs (100 μg/mL) treated with H_2O_2 (100 μM) in faintly acidic PBS (pH 5.5). The optical absorption curves under different time were detected through UV–vis spectroscopy.

2.7. Cell culture

Human normal liver cells (L02, ATCC, Manassas, VA) and human ovarian cancer cells (SKOV3, ATCC, Manassas, VA) were obtained from American Type Culture Collection (ATCC, Manassas, VA). L02 and SKOV3 were cultured in a humidified incubator (Thermo Fisher Scientific Inc. USA) with 5% CO_2 at 37 °C in normal RPMI-1680 medium (Hyclone) with 10% fetal bovine serum (FBS, Hyclone) and 1% penicillin-streptomycin.

2.8. In vitro safety and toxicity study

L02 cells and SKOV3 cells were seeded in 96-well plates at a density of 8000 cells per well and incubated overnight. After that, Cells were treated with different concentrations of EGCG and FeE@PEG NPs for 24 h, respectively. Then, the cell viability was measured using CCK-8 Assay following the manufacturer's instructions. Three parallel experiments were carried out.

2.9. Intracellular •OH detection

In order to test the generation of ROS by EGCG, and FeE@PEG NPs, DCFH-DA was used as the probe to detect intracellular ROS. SKOV3 cells suspension was seed into confocal Petri dishes. After incubation for 24 h at 37 °C, the cells were treated with PBS (control), EGCG (18.56 μg/mL) and FeE@PEG NPs (80 μg/mL) and then co-cultured for 4 h under 5% carbon dioxide incubator. After incubating with DCFH-DA (0.05 mM) of all groups of cells for 30 min in dark, the cells washed by PBS three times. The green fluorescence of DCF ($\lambda_{ex} = 488$ nm, $\lambda_{em} = 525$ nm) was observed by the confocal laser scanning microscope (CLSM) to evaluate the level of intracellular ROS.

2.10. Intracellular GSH detection

Intracellular GSH depletion measurement was with the aid of the GSH assay kit. SKOV3 cells were seeded into 6 well-plates. After incubation for 24 h at 37 °C, cells treated with PBS (control) and FeE@PEG NPs (80 μg/mL) . After 12 h, the cells were washed by PBS and collected through centrifugation (3000 rpm, 10 min, 4 °C). The contents of GSH was measured using GSH Assay Kit according to the manufacturer's instructions. The depletion of intracellular GSH was measured by the microplate reader. Three parallel experiments were carried out.

2.11. Western blot analysis

SKOV3 cells were seeded in 6-well plates. After incubation for 24 h at 37 °C, the cells were treated with PBS (control), EGCG (18.56 μg/mL) and FeE@PEG NPs (80 μg/mL) and then co-cultured for 24 h under 5% carbon dioxide incubator. Then, the treated cells were washed with PBS three times and collected by trypsinization and centrifugation for evaluating GPX4 expression by western bolt analysis.

2.12. Intracellular endocytosis

SKOV3 and L02 cells were plated in a 6-well plate. After incubation for 24 h at 37 °C, the cells were incubated with FeE@PEG NPs (80 μg/mL) at various times (0, 3, 6, 12 and 24 h). PBS washed away the uninternalized FeE@PEG NPs, and cells were dissolved through the cell lysate. The contents of iron were measured by inductively coupled plasma mass spectrometry (ICP-MS). Three parallel experiments were carried out.

2.13. Mitochondrial membrane potential detection

JC-1 fluorescent probe was employed to detect the change of mitochondrial membrane potential. SKOV3 cells suspension was seed into confocal Petri dishes. After incubation for 24 h at 37 °C, the cells were treated with PBS (control), EGCG (18.56 μg/mL) and FeE@PEG NPs (80 μg/mL) and then co-cultured for 24 h under 5% carbon dioxide incubator. Next, all cells washed by PBS and stained with stained with JC-1 for 25 min in dark, then the cells fluorescence images were collected by CLSM.

2.14. Apoptosis assay

Apoptosis of SKOV3 cells was measured using the one-step TUNEL Apoptosis Assay Kit. SKOV3 cells suspension was seed into confocal Petri dishes. After incubation for 24 h at 37 °C, the cells were treated with PBS (control), EGCG (18.56 μg/mL) and FeE@PEG NPs (80 μg/mL) and then co-cultured for 24 h under 5% carbon dioxide incubator. Next, all cells washed by PBS and stained with stained with TUNEL for 25 min in dark. The apoptosis signal of cells was observed by CLSM.

In addition, Apoptosis of SKOV3 cells was also verified by the Annexin V-FITC/PI Apoptosis Detection Kit. SKOV3 cells were seeded in 6-well plates. After incubation for 24 h at 37 °C, the cells were treated with PBS (control), EGCG (18.56 μg/mL) and FeE@PEG NPs (80 μg/mL) and then co-cultured for 24 h under 5% carbon dioxide incubator. The subsequent procedures were performed according to the manufacturer's protocol, and quantitative apoptotic measurements were performed by flow cytometric analysis.

2.15. Animal experiments

All animal procedures were performed in accordance with the Guidelines for Care and Use of Laboratory Animals of Fuzhou University and approved by the Animal Ethics Committee of Fuzhou University. BALB/c mice (18–20 g) were used for testing the biocompatibility and antitumoral effect of FeE@PEG NPs in vivo. All of the mice were purchased from Shanghai SLAC Laboratory Animal Co., Ltd. The tumors were established by subcutaneously injecting with the suspension of SKOV3 cells (5×10^6 cells/mL) into the right leg of the mice.

2.16. Hemolysis test

Blood was obtained from BALB/c mice and anticoagulated with ethylene diamine tetraacetic acid. The red blood cells (RBCs) were isolated from serum by centrifugation (2000 rpm, 2 min) and washed with PBS until the supernatant was clear. Next, 200 μL of the diluted RBCs suspension was added to 0.8 mL of PBS, H_2O, and different concentrations of FeE@PEG NPs (10, 25, 50, 75, 100 μg/mL). PBS group and H_2O group were used as the negative control (0% hemolysis) and the positive control (100% hemolysis), respectively. After treating for 4 h, the samples were centrifugated at 2000 rpm for 2 min, and the supernatant fluids were collected. The absorbance value at 541 nm of the supernatant fluids was measured by the UV–vis spectrometer. Three parallel experiments were carried out.

2.17. In vivo pharmacokinetics and biodistribution study

When the tumor volume reached 150 mm^3, tumor-bearing mice were intravenously injected with 200 μL of FeE@PEG NPs (2 mg/mL). 24 h and 48 h later, tumors and main organs (heart, liver, spleen, lung, and kidney) were collected and weighted. The blood was collected after intravenous injecting nanocomplexes for 3, 6, 12, 24, and 48 h. The contents of iron in each group were detected by ICP-MS.

2.18. In vivo antitumor activity study

The mice were randomly divided into three groups (n = 5). When the tumor volume reached 110 mm^3, the mice were intravenously injected with PBS (control), EGCG and FeE@PEG NPs. During the treatment, the tumor size and the body weight of each mouse were measured every two days. The tumor volume was quantified by formula $V = L \times W^2/2$ (L, the longest dimension; W, the shortest dimension). After keeping for 14 days, the mice were executed. The tumors and main organs were excised for hematoxylin and eosin (H&E) and terminal deoxynucleotidyl transferase-mediated dUTP nick-end labeling (TUNEL) staining assay.

3. Results and discussion

3.1. Preparation and characterization of FeE@PEG NPs

FeE NPs were prepared by a convenient coordination assembly process between iron ions and EGCG. In order to obtain the optimized nanocomplexes, the molar ratios of the reaction substrates were screened. As shown in Fig. S1, the FeE NPs gradually changed from regular nanocomplexes to disordered and heavily complexed morphology as the feeding ratio gradually increased. When Fe $(NO_3)_3 \bullet 9H_2O$:EGCG (mol: mol) = 0.36: 1, FeE NPs with uniform spherical shape could be obtained (Fig. 1a and b). The hydrodynamic diameter and zeta potential of the obtained nanocomplexes about 153 nm and −27.40 mV, respectively (Figs. S2 and S3). To further improve the biocompatibility of FeE NPs, DSPE-PEG were grafted onto the surface of FeE NPs (FeE@PEG NPs). As shown in Fig. 1c, there was no significant change in the morphology of the nanocomplexes before and after the grafting of PEG. The presence of C, O and Fe elements in FeE@PEG NPs were further determined by elemental mapping and energy dispersive spectroscopy (EDS) (Fig. 1d). C 1s, O 1s and Fe 2p peaks were also detected in FeE@PEG NPs by X-ray photoelectron spectroscopy (XPS) analysis, which was consistent with the results of EDS analysis (Fig. 1e and S4). The high-resolution XPS spectrum divided the Fe 2p peak into two and was assigned to Fe^{3+} (724.9 eV) and Fe^{2+} (711.7 eV). Therefore, the FeE@PEG NPs could possess excellent catalytic capacity associated with multivalent Fe elements. As shown in Fig. 1f and S5, benzene ring skeleton vibration at 1650 cm^{-1}~1475 cm^{-1}, O–H tensile vibration at 3355 cm^{-1}, and C–O tensile vibration at 1222 cm^{-1} of the FTIR spectrum indicate that FeE@PEG NPs contains EGCG. C–O–C tensile vibration at 1089 cm^{-1} of the FTIR spectrum indicate that FeE NPs contains F127 which was the surfactant, and the dispersion of FeE NPs prepared with F127 as raw material was more uniform and not easy to agglomerate. In addition, C–H tensile vibration at 2880 cm^{-1} of the FTIR spectrum indicates that FeE NPs contained DSPE-PEG and the dispersion of FeE NPs prepared with DSPE-PEG was

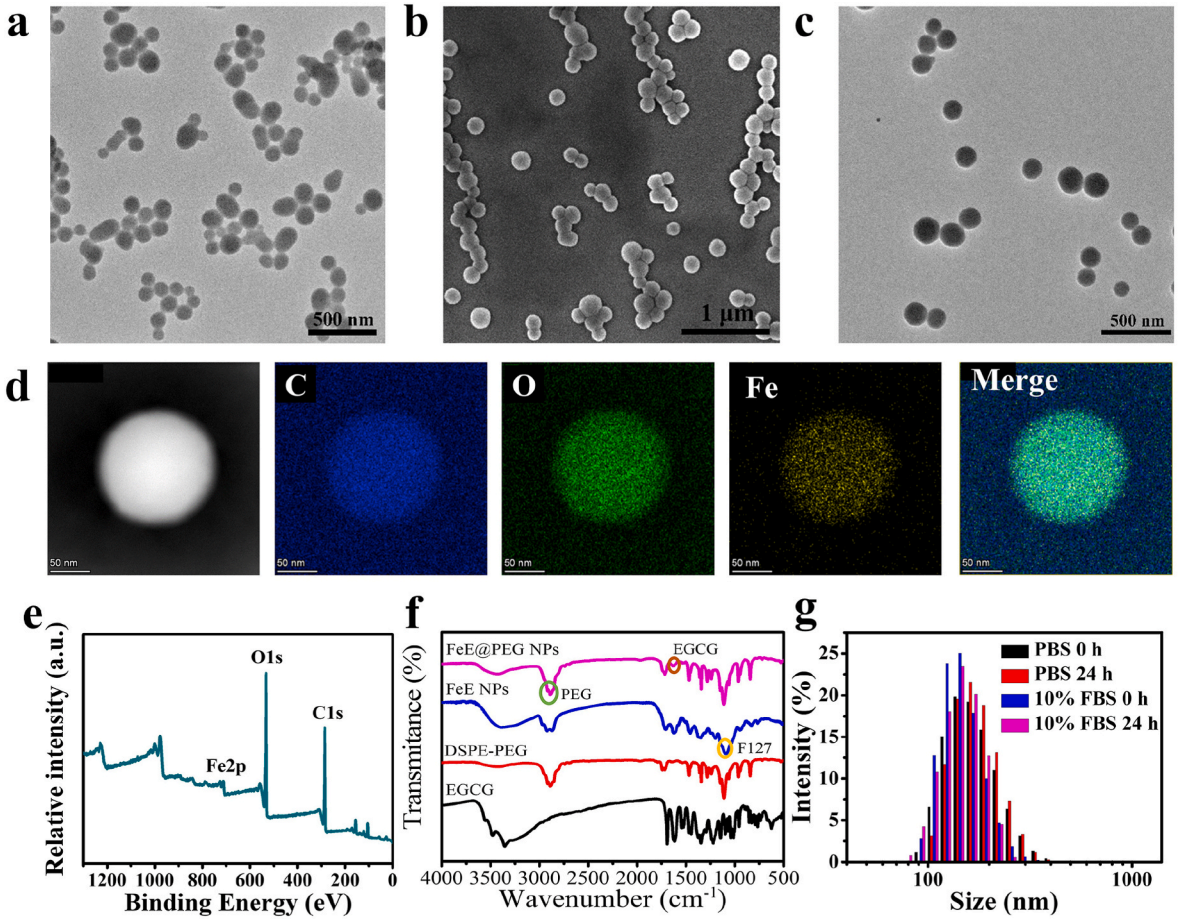

Fig. 1. (a) TEM image of FeE NPs. (b) SEM image of FeE NPs; (c) TEM image of FeE@PEG NPs. (d) High-angle annular dark-field-scanning TEM (HAADF-STEM) EDS elemental mapping images (for C, O and Fe) of FeE@PEG NPs. (e) XPS spectrum of FeE@PEG NPs. (f) FTIR spectra of EGCG, DSPE-PEG, FeN NPs and FeE@PEG NPs. (g) Hydrodynamic diameters of FeE@PEG NPs incubated with PBS or 10% FBS for different times.

good. The stability of FeE@PEG NPs in phosphate buffered saline (PBS) buffer or 10% fetal bovine serum (FBS) was investigated by dynamic light scattering (DLS) (Fig. 1g). The FeE@PEG NPs were stable in the different media for 24 h. In addition, FeE@PEG NPs were stable in PBS after 30 days (Fig. S6). Based on the absorption of EGCG at 505 nm, the loading capacity of EGCG was calculated as 23.17% (w/w, Fig. S7).

3.2. H_2O_2 responsiveness of FeE@PEG NPs

The ability of FeE@PEG NPs to be decomposed responsively in the TME was investigated. As shown in Fig. 2a and S8, FeE@PEG NPs partially decomposed in H_2O_2 solution. Furthermore, in the presence of both acidic environment (pH = 6.5) and H_2O_2, FeE@PEG NPs decomposed completely. The particle size of FeE@PEG NPs after complete decomposition was measured and found to have changed significantly compared to that before decomposition (Fig. 2b), which was consistent with the TEM images. Less than 10% of Fe can be released under PBS without H_2O_2 within 48 h, and 78% of Fe was released under H_2O_2 (Fig. S9). These results indicated that the highly oxidized environment in tumor cells could trigger the release of EGCG and iron ions to function accordingly.

3.3. Catalytic and auto-oxidation properties of FeE@PEG NPs

The ability of FeE@PEG NPs to catalyze the production of highly toxic •OH from H_2O_2 was a prerequisite for the activation of cellular ferroptosis. A typical TMB oxidation chromogenic assay was used to assess the •OH generation capacity. As shown in Fig. 2c, the UV–vis absorption curves of the solutions did not change significantly when H_2O_2 or FeE@PEG NPs were added alone. When H_2O_2 and FeE@PEG NPs were present together, a large amount of •OH was produced in the solution, which rapidly oxidized the TMB. The absorption intensities of oxTMB increased with the growth of H_2O_2 or FeE@PEG NPs concentrations (Fig. S10). The ability of FeE@PEG NPs was further investigated to catalyze the production of •OH from H_2O_2 by electron spin resonance (ESR) analysis. 5,5- Dimethyl-1-pyrroline N-oxide (DMPO) was applied as a trapping agent to monitor the production of •OH. As shown in Fig. 2d, there was no significant ESR signal when only H_2O_2 or FeE@PEG NPs were present in the solution. However, a clear quadruple peak was observed when both H_2O_2 and FeE@PEG NPs were present, demonstrating that FeE@PEG NPs catalyzed the Fenton reaction of H_2O_2 to produce a large amount of •OH.

EGCG, as a pro-oxidant, could enhance the Fenton reaction and improve the therapeutic effect of ferroptosis by increasing the level of endogenous H_2O_2 (Fig. S11). The auto-oxidation of FeE@PEG NPs produces H_2O_2 which was estimated by o-dianisidine reagent via absorption spectroscopy (Fig. 2e) [45]. The analysis was based on the transition of reduced o-dianisidine (colorless) to oxidized o-dianisidine (orange) by H_2O_2, which showed characteristic absorption at 460 nm. The results were shown that both EGCG and FeE@PEG NPs promoted the production of H_2O_2 (Fig. 2e). And with the increase of nanocomplexes concentration, the more H_2O_2 was produced. In addition, the fluorescent probe (pentafluorobenzenesulfonyl fluorescein, PBSF) was used to detect H_2O_2, which could emit green fluorescence after reacting with H_2O_2. Fluorescence spectra showed that H_2O_2 could be produced by EGCG (Fig. S12). This spontaneous production of H_2O_2 was beneficial to improve the therapeutic effect of ferroptosis. The UV–vis absorption spectra of TMB solution and ESR spectra were also proved that EGCG could promote the production of •OH by Fe^{3+} (Figs. S13 and S14).

In addition, it was important for tumor treatment by depleting the highly expressed intracellular GSH, which in turn leaded to redox imbalance and amplifies oxidative stress at the tumor cell. It was reported that 5,5′-Dithiobis-(2-nitrobenzoic acid) (DTNB) could react with sulfhydryl compounds to convert into the yellow product TNB [46]. Therefore, DTNB was used as an indicator to evaluate the ability of FeE@PEG NPs to deplete GSH. As shown in Fig. 2f, FeE@PEG NPs were able to oxidize a portion of the GSH. Additionally, the absorption spectrum changed significantly after adding FeE@PEG NPs, indicating that the GSH in the solution was depleted. This suggested that FeE@PEG NPs could effectively deplete intracellular GSH, which was favorable for increasing intracellular •OH and enhancing intracellular ferroptosis.

3.4. Cell uptake and in vitro cytotoxicity

The amount of nanocomplexes taken up by cells affected the final treatment effect to a certain extent. Then, the intracellular internalization of FeE@PEG NPs was studied via inductively coupled plasma-mass spectrometry (ICP-MS). Therefore, the uptake of FeE@PEG NPs by

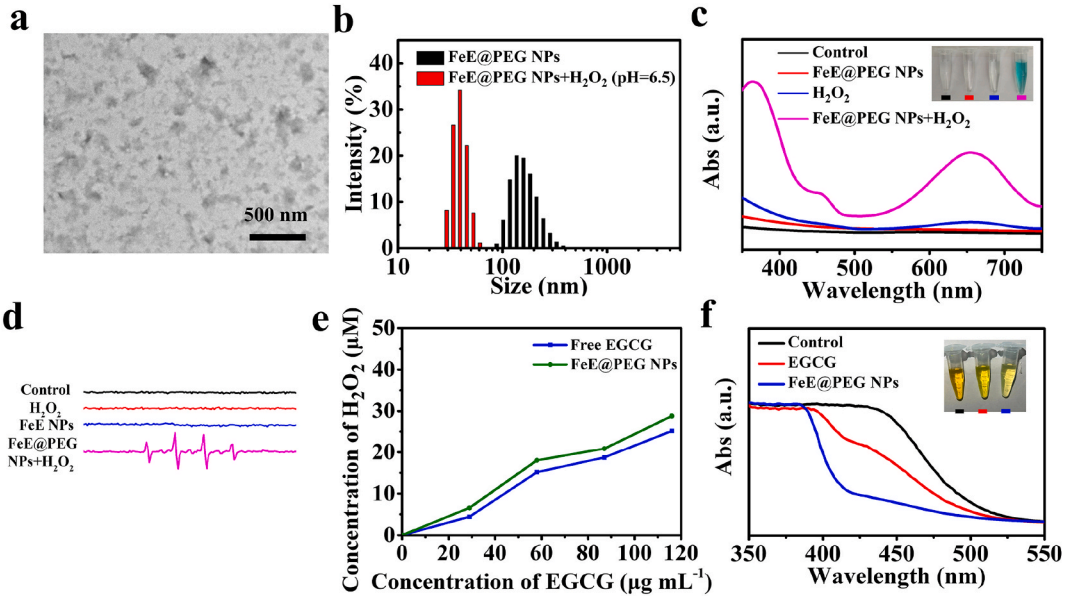

Fig. 2. (a) TEM image of FeE@PEG NPs after incubation with H_2O_2 for 1 h. (b) Hydrodynamic diameters of FeE@PEG NPs before and after incubation with H_2O_2 for 1 h. (c) The UV–vis absorption spectra of TMB aqueous solution with different treatments. (d) ESR spectroscopy of different reaction systems. (e) The ability to product H_2O_2 of FeE@PEG NPs and EGCG at different concentrations (f) Decrease of UV–Vis absorption at 410 nm showing the GSH depletion with different treatments.

human ovarian cancer SKOV3 cells and human normal liver cells L02 was investigated by incubation for different times (0, 3, 6, 12 and 24 h). The experimental results showed that the longer the incubation time, the higher uptake of FeE@PEG NPs by SKOV3 and L02 cells, which could reach about 17.2% and 15.6% at 24 h (Fig. 3a and S15). Effective uptake was an important prerequisite for the induction of tumor cell death by FeE@PEG NPs.

FeE@PEG NPs also had the ability to deplete intracellular GSH in the cells. As shown in Fig. 3b, intracellular GSH was measured to be depleted after incubated with EGCG/FeE@PEG NPs, demonstrating that EGCG and FeE@PEG NPs could effectively deplete the highly expressed GSH in tumor cells and achieve enhanced tumor treatment. Glutathione peroxidase 4 (GPX4), a key protein in scavenging ROS, could be inactivated and downregulated by ROS accumulation and GSH consumption, and eventually leading to ferroptosis. Therefore, the expression of GPX4 was investigated using western blot. Compared with the control and the treatment with EGCG alone, FeE@PEG NPs effectively downregulated the GPX4 level in SKOV3 cells, indicating the consumption of GSH (Fig. 3c and S16). The fluorescent probe PBSF was used to detect the formation of H_2O_2, which could emit green fluorescence after reacting with H_2O_2. SKOV3 cells incubated with EGCG under hypoxic conditions showed a stronger fluorescence signal, indicating that H_2O_2 was generated intracellularly (Fig. S17). In addition, the change of intracellular ROS content was one of the important indicators of ferroptosis. The level of intracellular ROS could be assessed by using 2′,7′-Dichlorodihydrofluorescein diacetate (DCFH-DA) as a probe of ROS. When ROS was produced inside the cell, DCFH-DA was oxidized and exhibited green fluorescence. As shown in Fig. 3d, EGCG could activate cascade reactions to elevate the intracellular H_2O_2 level, facilitating ferroptosis. SKOV3 cells incubated with FeE@PEG NPs showed a stronger fluorescence signal, indicating that a large amount of •OH was generated intracellularly. Meanwhile, cellular lipid peroxides (LPO) were important markers of ferroptosis. LPO fluorescent probe (Liperfluo) was used to detect the contents of LPO in SKOV3 cells treated with Control (PBS), EGCG and FeE@PEG NPs. As shown in Fig. 3e, FeE@PEG NPs treated SKOV3 cells showed a stronger green fluorescence than EGCG and control. This suggested that FeE@PEG NPs had a stronger effect on

inducing ferroptosis in tumor cells. To further confirm the induction of ferroptosis, the contents of malondialdehyde (MDA) (aldehyde secondary product of lipid peroxidation) were also examined in treated tumor cells. As shown in Fig. S18, SKOV3 cells treated by FeE@PEG NPs clearly exhibited more MDA compared to control or EGCG treated cells. Thus, FeE@PEG NPs may lead to preferential killing of tumor cells by synergistically generating ROS and inhibiting the antioxidant system.

After demonstrating the Fenton catalytic effects and H_2O_2 production properties of the FeE@PEG NPs, their antitumor effects of FeE@PEG NPs were investigated at the cellular level. FeE@PEG NPs exhibited responsive disassembly in TME with overexpressing H_2O_2. The impact of EGCG and FeE@PEG NPs on cell viability was assessed using CCK-8

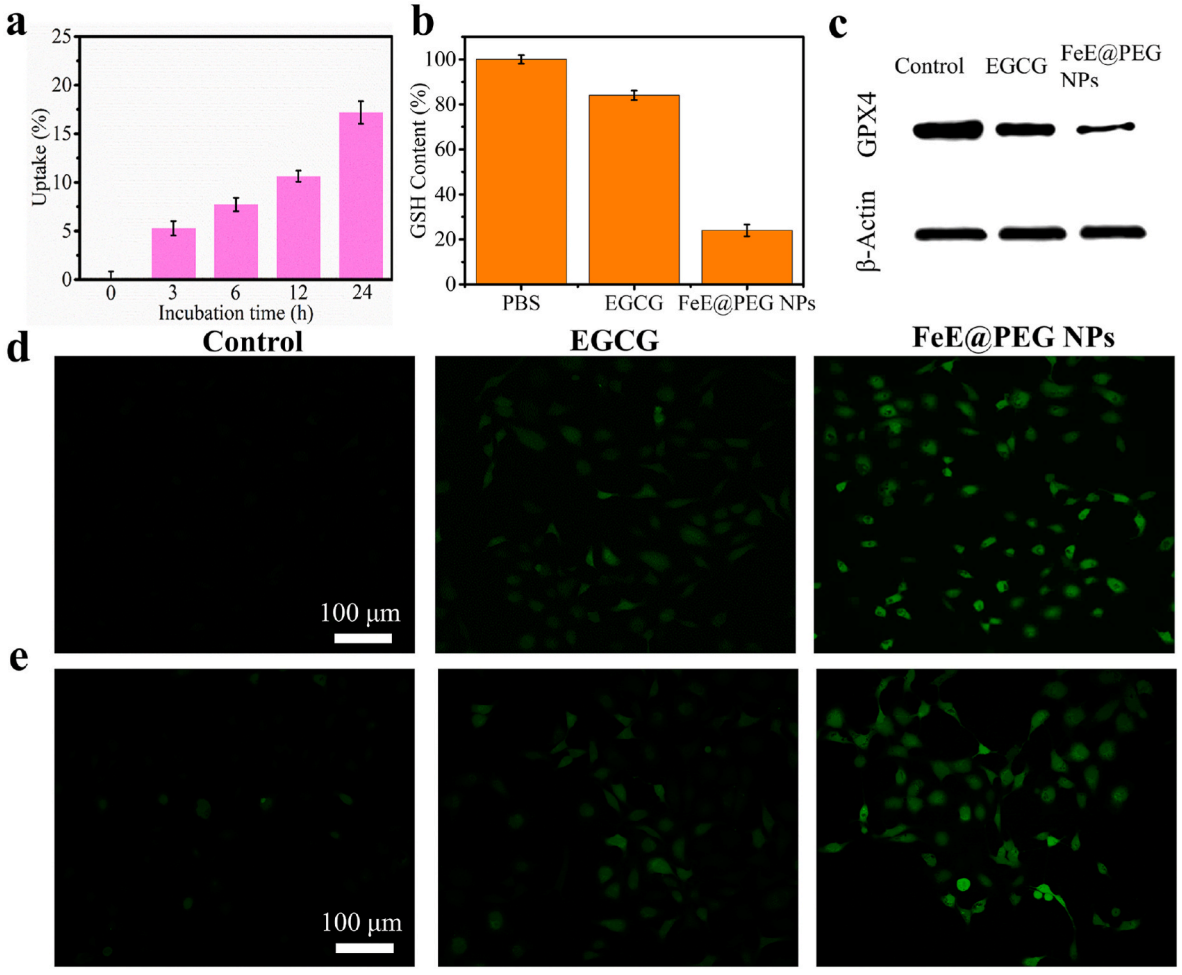

Fig. 3. (a) Intracellular internalization of FeE@PEG NPs after incubating with SKOV3 cells for 0, 3, 6, 12 and 24 h, respectively. (b) Intracellular GSH depletion of SKOV3 cells after incubation with EGCG and FeE@PEG NPs for 12 h. (c) Western blot image of the expression of GPX4 with different treatments. (d) CLSM of SKOV3 cells stained with DCFH-DA after different treatments for 4 h. (e) CLSM of SKOV3 cells stained with Liperfluo after different treatment for 4 h. Data represent mean values ± s.d., n = 3.

assay for human normal hepatic L02 cells and human ovarian cancer SKOV3 cells. (Fig. 4a and b). When L02 cells were incubated with FeE@PEG NPs for 24 h, FeE@PEG NPs had low biotoxicity and the cells remained in a normal growth state. In contrast, the survival rate of SKOV3 cells incubated with FeE@PEG NPs (80 μg/mL) was only about 15.5%. These results suggested that FeE@PEG NPs specifically kill tumor cells, while having a good biosafety for normal cells. To visualize the distribution of dead and live cells, Calcein-AM/PI double staining experiments were performed on both cells. L02 cells and SKOV3 cells were incubated with EGCG (18.56 μg/mL) and FeE@PEG NPs (80 μg/mL) for 24 h, respectively, followed by cell staining (Fig. 4c). No obvious death signal was found in L02 cells, while almost all SKOV3 cells died after incubation with FeE@PEG NPs, which was consistent with the experimental results of CCK-8.

Next, the intracellular mitochondrial membrane potential was explored to determine cell death. The mitochondrial membrane potential (MMP) of normal growth cells was relatively high positive potential. Mitochondria showed red fluorescence after staining with MMP characteristic dye 5,5′,6,6′-tetrachloro-1,1′,3,3′-tetraethylbenzimidazolylcarbocyanine iodide (JC-1). When cells died, MMP decreased and JC-1 was displayed green fluorescence on mitochondria. As shown in Fig. 4d, SKOV3 cells showed green fluorescence after incubated with FeE@PEG NPs, which meant FeE@PEG NPs could cause changes in MMP. The TEM images of the cells also showed that the mitochondrial volume decreased and the mitochondrial membrane density increased after incubation with FeE@PEG NPs, which was a characteristic of ferroptosis (Fig. S19). In addition, the chromosomal DNA in the nucleus would be broken into DNA fragments in the late stage of apoptosis, which could be detected by the terminal deoxynucleotidyl transferase dUTP nick end labeling (TUNEL) assay. After incubation with FeE@PEG NPs, SKOV3 cells exhibited the appearance of red fluorescence, which meant there were DNA fragments in SKOV3 cells (Fig. 4e). The FITC-Annexin V/PI method was also taken to verify the occurrence of the above cell death process. As can be observed in Fig. 4f, almost no apoptosis occurred in the control group. In contrast, the mortality rate increased to 94.11% in the FeE@PEG NPs-treated group. This was consistent with the results of the above apoptosis experiments.

3.5. Biodistribution of FeE@PEG NPs in vivo

Before in vivo treatment, the biocompatibility of FeE@PEG NPs was assessed by using a hemolysis assay. As shown in Fig. S20, the low erythrocyte hemolytic toxicity demonstrated the biocompatibility of FeE@PEG NPs and its potential for further application in intravenous therapy in vivo. In addition, a systematic study of the biodistribution of FeE@PEG NPs in major organs and tumor sites was performed. As shown in Fig. S21, FeE@PEG NPs could effectively accumulate in tumor sites. The in vivo circulation half-life of the FeE@PEG NPs was about 7 h (Fig. S22).

3.6. In vivo antitumor effects of FeE@PEG NPs

SKOV3 tumor-bearing mice were used as an in vivo tumor model to assess the specific killing ability of FeE@PEG NPs on tumor tissues.

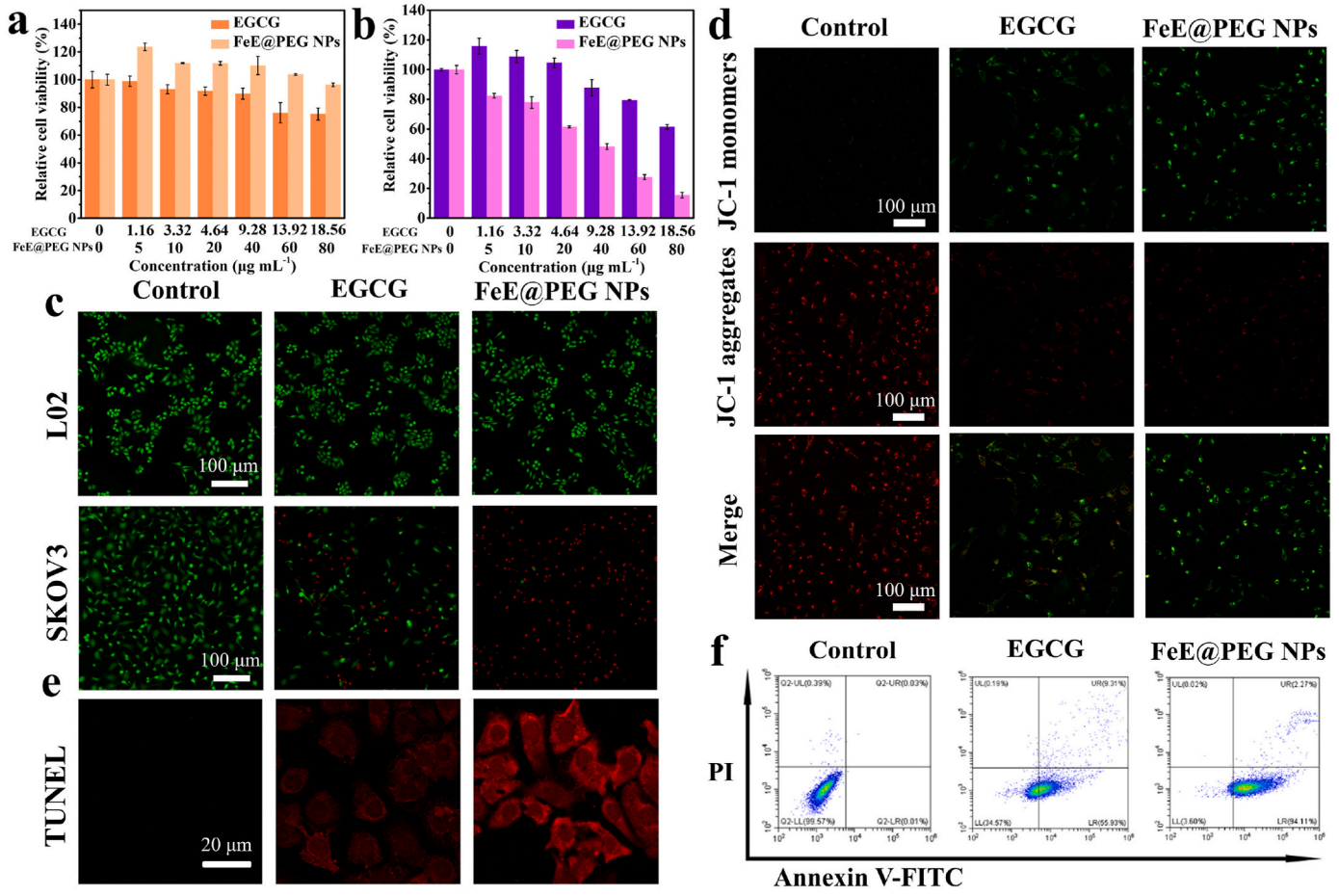

Fig. 4. Relative cell viabilities of (a) L02 and (b) SKOV3 cells after incubation with EGCG and FeE@PEG NPs for 24 h. (c) Live/dead staining of L02 and SKOV3 cells after incubation with different treatments for 24 h. (d) JC-1 determining the mitochondrial membrane potential changes after treatment of SKOV3 cells with EGCG, and FeE@PEG NPs for 24 h. (e) TUNEL assay of SKOV3 cells after different treatments for 24 h. (f) Flow cytometry of SKOV3 cells after different treatments for 24 h. Data represent mean values ± s.d., n = 3.

Tumor-bearing mice with tumor volumes around 110 mm^3 were randomly divided into three groups (n = 5 per group). The corresponding nanocomplexes was injected into the tail vein of the three groups every two days, and the body weight of the mice was also recorded. The results showed that the body weights of the mice in all three groups did not change significantly during the 14-day treatment period, indicating that FeE@PEG NPs did not cause any major side effects (Fig. 5a). As shown in Fig. 5b–c, the tumors of the control group grew rapidly over time. FeE@PEG NPs inhibited the tumor growth most effectively, with the tumor inhibition rate around 90%. FeE@PEG NPs could effectively prolong the survival time of mice (Fig. S23). In addition, the contents of GSH and the expression of GPX4 in the post-treatment tumor tissues were decreased, which indicated that FeE@PEG NPs could induce ferroptosis in tumor tissues (Figs. S24 and S25). The results of H&E staining and TUNEL staining also showed that the tumors slices of FeE@PEG NPs group showed significant cell damage, indicating that FeE@PEG NPs could effectively induce tumor cell death (Fig. 5d–e). The results of immunohistochemistry (CD3, CD8, CD11) indicated that ferroptosis induced by FeE@PEG NPs could induce a certain immune response (Fig. S26). To further determine that FeE@PEG NPs did not affect the function of normal organs and tissues, H&E staining was performed on different organs after euthanasia of mice. As shown in Fig. S27, there was no significant difference between the sections of each organ in the FeE@PEG NPs group compared with the control group, indicating that FeE@PEG NPs had no significant pathological toxic effects on the major organs of the mice in each group, suggesting that FeE@PEG NPs has a relatively high biosafety.

4. Conclusion

In summary, we obtained an H_2O_2-responsive ferroptosis-inducing platform FeE@PEG NPs to synergistically initiate the iron-dependent Fenton reaction and attenuate antioxidant activities for improved tumor ferroptosis therapy. The results demonstrated that the carrier-free FeE@PEG NPs could be disassembled by H_2O_2 in the TME and rapidly release EGCG and Fe^{3+}. The released Fe^{3+} produces large amounts of toxic •OH by the Fenton reactions while having minimal impact on normal cells. The generated •OH effectively induces lipid peroxidation, which leads to ferroptosis in tumor cells. In addition, EGCG can autoxidize producing H_2O_2, which further promotes •OH production and LPO production. Moreover, EGCG could deplete high levels of intracellular GSH and inhibit the antioxidant systems, triggering LPO accumulation via blocking the repair process of oxidized lipids. This study provides new insights into advancing anticancer ferroptosis through rational material design, offering promising avenues for future research.

Authors' contributions

M. W. and A. Y. conceived and designed this project. M. W., Y. A. and W. H. performed cellular and animal experiments. M. W. and J. C. carried out the synthesis of all compounds. M. W., A. Y., W. H., J. C. and X. T. analyzed and discussed the results. X. X., J. C., C. L. and X. T provided important comments on this project. M. W. and C. L. drafted this manuscript. All authors discussed the data and contributed to the editing of the manuscript.

CRediT authorship contribution statement

Min Wang: Writing – review & editing, Writing – original draft, Data curation, Conceptualization. **Aoling Yu:** Data curation, Conceptualization. **Wen Han:** Data curation. **Jingyi Chen:** Data curation. **Chunhua Lu:** Writing – review & editing, Writing – original draft, Data curation. **Xiankun Tu:** Writing – review & editing, Writing – original draft.

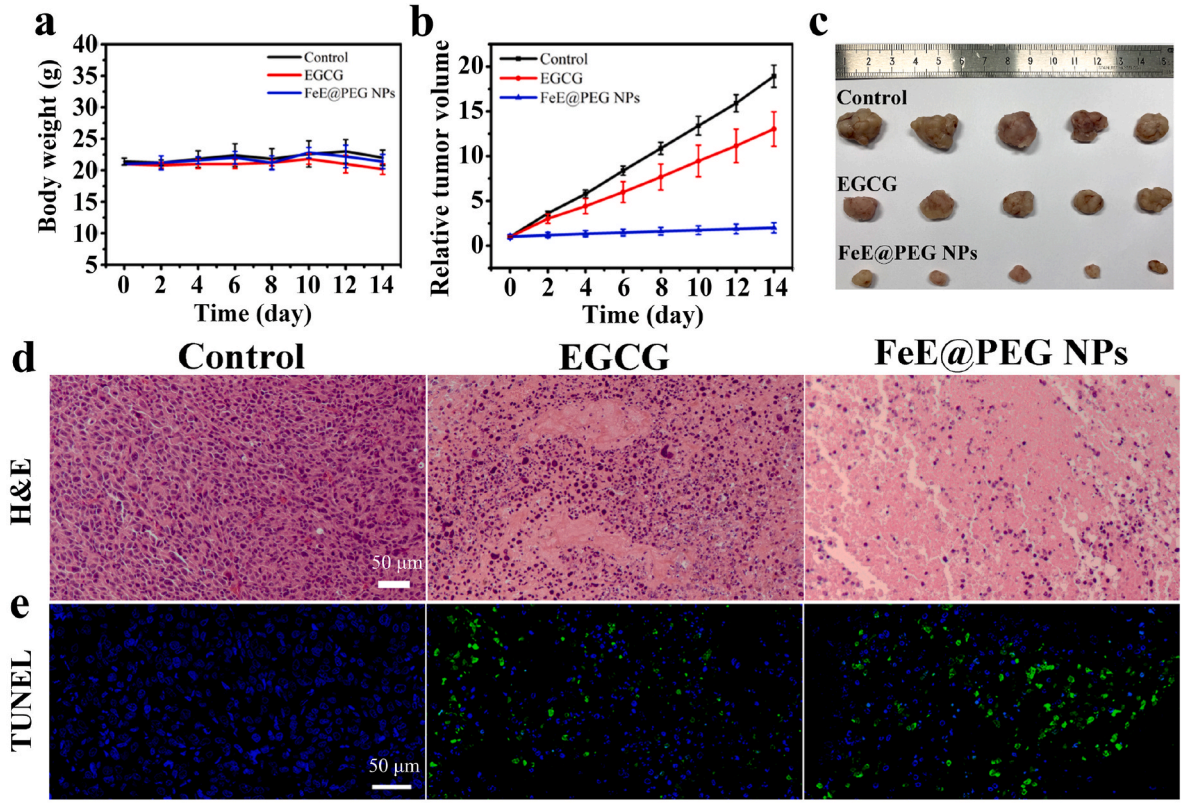

Fig. 5. (a) Time-dependent bodyweight curves for nude mice bearing SKOV3 cells after intravenous injection of EGCG, and FeE@PEG NPs. (b) Time-dependent tumor growth curves for nude mice bearing SKOV3 cells under different treatments. (c) Visual image of excised tumor after different treatments on the 14th day. (d) H&E and (e) TUNEL staining of tumor tissues of nude mice bearing SKOV3 cells after different treatments. Data represent mean values ± s.d., n = 5.

Declaration of competing interest

The authors declare that they have no known competing financial interests or personal relationships that could have appeared to influence the work reported in this paper.

Data availability

Data will be made available on request.

Acknowledgments

This research was supported by the National Key R&D Program of China (No. 2018YFA0902600), the National Natural Science Foundation of China (No. 22174019), the Natural Science Foundation of Fujian (No. 2020J06036), Excellent Young Scholars Cultivation Project of Fujian Medical University Union Hospital (No. 2022XH040).

Appendix A. Supplementary data

Supplementary data to this article can be found online at doi: mmcdoino

References

[1] B.R. Stockwell, J.P. Friedmann Angeli, H. Bayir, A.I. Bush, M. Conrad, S.J. Dixon, S. Fulda, S. Gascon, S.K. Hatzios, V.E. Kagan, K. Noel, X. Jiang, A. Linkermann, M. E. Murphy, M. Overholtzer, A. Oyagi, G.C. Pagnussat, J. Park, Q. Ran, C. S. Rosenfeld, K. Salnikow, D. Tang, F.M. Torti, S.V. Torti, S. Toyokuni, K. A. Woerpel, D.D. Zhang, Ferroptosis: a regulated cell death nexus linking metabolism, Redox Biology, and Disease, Cell 171 (2) (2017) 273–285.
[2] M. Liu, B. Liu, Q.Q. Liu, K.K. Du, Z.F. Wang, N.Y. He, Nanomaterial-induced ferroptosis for cancer specific therapy, Coord. Chem. Rev. 382 (2019) 160–180.
[3] X. Chen, R. Kang, G. Kroemer, D. Tang, Broadening horizons: the role of ferroptosis in cancer, Nat. Rev. Clin. Oncol. 18 (5) (2021) 280–296.
[4] M. Conrad, D.A. Pratt, The chemical basis of ferroptosis, Nat. Chem. Biol. 15 (12) (2019) 1137–1147.
[5] Q. Liu, Y. Zhao, H. Zhou, C. Chen, Ferroptosis: challenges and opportunities for nanomaterials in cancer therapy, Regen. Biomater. 10 (2023) rbad004.
[6] K. Newton, A. Strasser, N. Kayagaki, V.M. Dixit, Cell death, Cell 187 (2) (2024) 235–256.
[7] D. Li, Y. Li, The interaction between ferroptosis and lipid metabolism in cancer, Signal Transduct, Target Ther. 5 (1) (2020) 108.
[8] C. Liang, X. Zhang, M. Yang, X. Dong, Recent progress in ferroptosis inducers for cancer therapy, Adv. Mater. 31 (51) (2019) e1904197.
[9] P. Zhang, Y. Hou, J. Zeng, Y. Li, Z. Wang, R. Zhu, T. Ma, M. Gao, Coordinatively unsaturated Fe3+ based activatable probes for enhanced MRI and therapy of tumors, Angew. Chem., Int. Ed. Engl. 58 (32) (2019) 11088–11096.
[10] Y. Wang, J. Hu, S. Wu, J.S. Fleishman, Y. Li, Y. Xu, W. Zou, J. Wang, Y. Feng, J. Chen, H. Wang, Targeting epigenetic and posttranslational modifications regulating ferroptosis for the treatment of diseases, Signal Transduct. Targeted Ther. 8 (1) (2023) 449.
[11] X. Jiang, Q. Peng, M. Peng, L. Oyang, H. Wang, Q. Liu, X. Xu, N. Wu, S. Tan, W. Yang, Y. Han, J. Lin, L. Xia, Y. Tang, X. Luo, J. Dai, Y. Zhou, Q. Liao, Cellular metabolism: a key player in cancer ferroptosis, Cancer Commun. 44 (2) (2024) 185–204.
[12] B. Qiu, F. Zandkarimi, C.T. Bezjian, E. Reznik, R.K. Soni, W. Gu, X. Jiang, B. R. Stockwell, Phospholipids with two polyunsaturated fatty acyl tails promote ferroptosis, Cell 187 (5) (2024) 1177–1190.
[13] F. Zhang, F. Li, G.H. Lu, W. Nie, L. Zhang, Y. Lv, W. Bao, X. Gao, W. Wei, K. Pu, H. Y. Xie, Engineering magnetosomes for ferroptosis/immunomodulation synergism in cancer, ACS Nano 13 (5) (2019) 5662–5673.
[14] H. He, L. Du, H. Guo, Y. An, L. Lu, Y. Chen, Y. Wang, H. Zhong, J. Shen, J. Wu, X. Shuai, Redox responsive metal organic framework nanoparticles induces ferroptosis for cancer therapy, Small 16 (33) (2020) e2001251.
[15] T. Liu, W. Liu, M. Zhang, W. Yu, F. Gao, C. Li, S.B. Wang, J. Feng, X.Z. Zhang, Ferrous-supply-regeneration nanoengineering for cancer-cell-specific ferroptosis in combination with imaging-guided photodynamic therapy, ACS Nano 12 (12) (2018) 12181–12192.
[16] J. Yu, F. Zhao, W. Gao, X. Yang, Y. Ju, L. Zhao, W. Guo, J. Xie, X.J. Liang, X. Tao, J. Li, Y. Ying, W. Li, J. Zheng, L. Qiao, S. Xiong, X. Mou, S. Che, Y. Hou, Magnetic reactive oxygen species nanoreactor for switchable magnetic resonance imaging guided cancer therapy based on pH-sensitive Fe(5)C(2)@Fe(3)O(4) nanoparticles, ACS Nano 13 (9) (2019) 10002–10014.
[17] W. Feng, W. Shi, Z. Wang, Y. Cui, X. Shao, S. Liu, L. Rong, Y. Liu, H. Zhang, Enhancing tumor therapy of Fe(III)-Shikonin supramolecular nanomedicine via triple ferroptosis amplification, ACS Appl. Mater. Interfaces 14 (33) (2022) 37540–37552.
[18] Y. Guo, H. Luo, H. Jiang, X. Liu, X. Long, Y. Hou, Z. Chen, Y. Sun, D. Ge, W. Shi, Liposome encapsulated polydopamine nanoparticles: enhancing ferroptosis and activating hypoxia prodrug activity, Mater. Today Bio 25 (2024) 101009.
[19] L.H. Fu, C. Qi, Y.R. Hu, J. Lin, P. Huang, Glucose oxidase-instructed multimodal synergistic cancer therapy, Adv. Mater. 31 (21) (2019) e1808325.
[20] S. Wang, Z. Wang, G. Yu, Z. Zhou, O. Jacobson, Y. Liu, Y. Ma, F. Zhang, Z.Y. Chen, X. Chen, Tumor-specific drug release and reactive oxygen species generation for cancer chemo/chemodynamic combination therapy, Adv. Sci. 6 (5) (2019) 1801986.
[21] L.S. Lin, T. Huang, J. Song, X.Y. Ou, Z. Wang, H. Deng, R. Tian, Y. Liu, J.F. Wang, Y. Liu, G. Yu, Z. Zhou, S. Wang, G. Niu, H.H. Yang, X. Chen, Synthesis of copper peroxide nanodots for H(2)O(2) self-supplying chemodynamic therapy, J. Am. Chem. Soc. 141 (25) (2019) 9937–9945.
[22] L.L. Zhou, Q. Guan, W.Y. Li, Z. Zhang, Y.A. Li, Y.B. Dong, A ferrocene-functionalized covalent organic framework for enhancing chemodynamic therapy via redox dyshomeostasis, Small 17 (32) (2021) e2101368.
[23] B. Yu, B. Choi, W. Li, D.H. Kim, Magnetic field boosted ferroptosis-like cell death and responsive MRI using hybrid vesicles for cancer immunotherapy, Nat. Commun. 11 (1) (2020) 3637.
[24] V. Aggarwal, H.S. Tuli, M. Tania, S. Srivastava, E.E. Ritzer, A. Pandey, D. Aggarwal, T.S. Barwal, A. Jain, G. Kaur, K. Sak, M. Varol, A. Bishayee, Molecular mechanisms of action of epigallocatechin gallate in cancer: recent trends and advancement, Semin. Cancer Biol. 80 (2022) 256–275.
[25] K. Li, G. Xiao, J.J. Richardson, B.L. Tardy, H. Ejima, W. Huang, J. Guo, X. Liao, B. Shi, Targeted therapy against metastatic melanoma based on self-assembled metal-phenolic nanocomplexes comprised of green tea catechin, Adv. Sci. 6 (5) (2019) 1801688.
[26] B. Hu, S.J. Yu, C. Shi, J. Gu, Y. Shao, Q. Chen, Y.Q. Li, R. Mezzenga, Amyloid-polyphenol hybrid nanofilaments mitigate colitis and regulate gut microbial dysbiosis, ACS Nano 14 (3) (2020) 2760–2776.
[27] K. Liang, J.E. Chung, S.J. Gao, N. Yongvongsoontorn, M. Kurisawa, Highly augmented drug loading and stability of micellar nanocomplexes composed of doxorubicin and poly(ethylene glycol)-green tea catechin conjugate for cancer therapy, Adv. Mater. 30 (14) (2018) e1706963.
[28] P. Davoodi, L.Y. Lee, Q. Xu, V. Sunil, Y. Sun, S. Soh, C.H. Wang, Drug delivery systems for programmed and on-demand release, Adv. Drug Deliv. Rev. 132 (2018) 104–138.
[29] W.W. Shen, R.J. Wang, Q.Q. Fan, Y.W. Li, Y.Y. Cheng, Natural polyphenol assisted delivery of single-strand oligonucleotides by cationic polymers, Gene Ther. 27 (7–8) (2020) 383–391.
[30] N. Yongvongsoontorn, J.E. Chung, S.J. Gao, K.H. Bae, A. Yamashita, M.H. Tan, J. Y. Ying, M. Kurisawa, Carrier-enhanced anticancer efficacy of sunitinib-loaded green tea-based micellar nanocomplex beyond tumor-targeted delivery, ACS Nano 13 (7) (2019) 7591–7602.
[31] T. Liang, Z. Yao, J. Ding, Q. Min, L. Jiang, J.J. Zhu, Cascaded aptamers-governed multistage drug-delivery system based on biodegradable Envelope-Type Nanovehicle for targeted therapy of HER2-overexpressing breast cancer, ACS Appl. Mater. Interfaces 10 (40) (2018) 34050–34059.
[32] X. Wang, J.-J. Yan, L. Wang, D. Pan, R. Yang, Y. Xu, J. Sheng, Q. Huang, H. Zhao, M. Yang, Rational design of polyphenol-poloxamer nanovesicles for targeting inflammatory bowel disease therapy, Chem. Mater. 30 (12) (2018) 4073–4080.
[33] D. Chuan, H. Hou, Y. Wang, M. Mu, J. Li, Y. Ren, N. Zhao, B. Han, H. Chen, G. Guo, Multifunctional metal-polyphenol nanocomposite for melanoma targeted photo/chemodynamic synergistic therapy, J. Mater. Sci. Technol. 152 (2023) 159–168.
[34] L. Xie, J. Li, G. Wang, W. Sang, M. Xu, W. Li, J. Yan, B. Li, Z. Zhang, Q. Zhao, Z. Yuan, Q. Fan, Y. Dai, Phototheranostic metal-phenolic networks with antiexosomal PD-L1 enhanced ferroptosis for synergistic immunotherapy, J. Am. Chem. Soc. 144 (2) (2022) 787–797.
[35] Y. Xu, Y. Guo, C. Zhang, M. Zhan, L. Jia, S. Song, C. Jiang, M. Shen, X. Shi, Fibronectin-coated metal–phenolic networks for cooperative tumor chemo-/chemodynamic/immune therapy via enhanced ferroptosis-mediated immunogenic cell death, ACS Nano 16 (1) (2022) 984–996.
[36] Y. Guo, X. Zhang, S.-Z. Wang, H.-H. Feng, S.-Y. Wu, F.-G. Wu, Metal–phenolic network-facilitated "foe-to-friend" conversion of melittin for cancer immunotherapy with boosted abscopal effect, Research 6 (2023) 52.
[37] W. Xu, Z. Lin, S. Pan, J. Chen, T. Wang, C. Cortez-Jugo, F. Caruso, Direct assembly of metal-phenolic network nanoparticles for biomedical applications, Angew. Chem., Int. Ed. Engl. 62 (45) (2023) e202312925.
[38] J.D. Lambert, R.J. Elias, The antioxidant and pro-oxidant activities of green tea polyphenols: a role in cancer prevention, Arch. Biochem. Biophys. 501 (1) (2010) 65–72.
[39] A.J. León-González, C. Auger, V.B. Schini-Kerth, Pro-oxidant activity of polyphenols and its implication on cancer chemoprevention and chemotherapy, Biochem. Pharmacol. 98 (3) (2015) 371–380.
[40] T. Nakazato, K. Ito, Y. Ikeda, M. Kizaki, Green tea component, catechin, induces apoptosis of human malignant B cells via production of reactive oxygen species, Clin. Cancer Res. 11 (16) (2005) 6040–6049.
[41] S. Gorlach, J. Fichna, U. Lewandowska, Polyphenols as mitochondria-targeted anticancer drugs, Cancer Lett. 366 (2) (2015) 141–149.
[42] Y. He, Z. Fan, P. Sun, H. Jiang, Z. Chen, G. Tang, Z. Hou, Y. Sun, Y. Yi, W. Shi, D. Ge, Mechanism of self-oxidative copolymerization and its application with polydopamine-pyrrole nano-copolymers, Small Methods (2024) 2301405.
[43] N.R. Unnadkat, R.J. Elias, Oxidative stability of (-)-epigallocatechin gallate in the presence of thiols, J. Agric. Food Chem. 60 (43) (2012) 10815–10821.

[44] W. Wang, Y. Jin, X. Liu, F. Chen, X. Zheng, T. Liu, Y. Yang, H. Yu, Endogenous stimuli-activatable nanomedicine for immune theranostics for cancer, Adv. Funct. Mater. 31 (26) (2021) 2100386.
[45] S. Sharma, D. Mittal, A.K. Verma, I. Roy, Copper-gallic acid nanoscale metal-organic framework for combined drug delivery and photodynamic therapy, ACS Appl. Bio Mater. 2 (5) (2019) 2092–2101.
[46] Z. Ren, S. Sun, R. Sun, G. Cui, L. Hong, B. Rao, A. Li, Z. Yu, Q. Kan, Z. Mao, A metal-polyphenol-coordinated nanomedicine for synergistic cascade cancer chemotherapy and chemodynamic therapy, Adv. Mater. 32 (6) (2020) e1906024.